MATERIALS CHEMISTRY FRONTIERS

CHINESE CHEMICAL SOCIETY

ROYAL SOCIETY OF CHEMISTRY

RESEARCH ARTICLE

View Article Online
View Journal | View Issue

Cite this: *Mater. Chem. Front.*, 2023, **7**, 1365

Bimetallic Ni–Co selenide heterostructure aerogel for highly efficient overall water splitting†

Hongchen Liu, Fan Yang,* Fengjiang Chen, Sai Che, Neng Chen, Chong Xu, Ni Wu, Wenkai Wei and Yongfeng Li*

Received 20th October 2022,
Accepted 23rd January 2023

DOI: 10.1039/d2qm01082h

rsc.li/frontiers-materials

Exploring transition metal-based electrocatalysts with excellent performance toward alkaline overall water splitting is of significant importance for the hydrogen economy but remains challenging. Herein, we designed and prepared a bimetallic Ni–Co selenide heterostructure aerogel ($NiSe_2$–$CoSe_2$) for highly efficient overall water splitting *via* facile spontaneous gelation and selenium vapor deposition. The optimized sample exhibited extremely low overpotentials of 65/220 mV for the HER/OER at a geometric current density of 10 mA cm^{-2} in 1 M KOH electrolyte. Assembled as an electrolyzer for overall water splitting, $NiSe_2$–$CoSe_2$ only required a low cell voltage of 1.56 V to achieve 10 mA cm^{-2} with decent stability, which was comparable to those of commercial noble-metal catalysts (Pt/C + RuO_2). The exceptional performance was attributed to the unique porous morphology of the aerogel with abundant active sites and the bimetallic selenide heterostructure with excellent intrinsic activity. Density functional theory (DFT) calculations further revealed the ideal adsorption performance for reactant intermediates at the heterogeneous phase boundaries. This work provides an anticipated perspective of transition metal selenide bifunctional electrocatalysts for overall water splitting.

Introduction

Nowadays, the ever-worsening global energy crisis and environmental pollution push the development of renewable energy, especially toward 'green hydrogen' produced by water splitting.[1,2] Currently, noble metal-based catalysts show the best performance for electrocatalytic water splitting with a low operating voltage. However, high cost and low reserves dramatically prevent their large-scale application.[3,4] In this case, the development of highly active non-noble metal electrocatalysts has been a hot research topic in recent years, such as transition metal (Ni, Co, or Fe, *etc.*) alloys[5–7] or compounds (phosphides, sulfides, selenides, nitrides or oxides, *etc.*).[8–12] Although some of the materials demonstrate electrocatalytic hydrogen or oxygen evolution reaction (HER or OER) activities comparable to those of precious metal catalysts, the research and applications of those materials in overall water splitting are insufficient. To this end, it is particularly crucial to design and develop bifunctional non-noble metal electrocatalysts with low overpotential and good stability for highly efficient overall water splitting.

Basically, high performance electrocatalysts for the HER require moderate adsorption/desorption properties with H*, while high performance electrocatalysts for the OER need balanced binding energy of O* between OH* and OOH*.[3,13] In this regard, transition metal-based selenides (TMSes) have been widely studied as a newly discovered family for water electrolysis owing to their unique features.[10] As sulfide analogs, TMSes have balanced hydrogen bonding energy, leading to favorable catalytic performance toward the HER.[14] Meanwhile, some TMSes with a cubic pyrite-type crystal structure (*e.g.* $NiSe_2$, $CoSe_2$, *etc.*) can efficiently coordinate with water/hydroxide and undergo oxidation and reduction on an anode to construct a oxide/hydroxide shell with advanced OER catalytic activity and stability.[15,16] Besides, the unique metal-like properties of selenium allow excellent electrical conductivity of TMSes, which leads to desirable charge transfer, reaction kinetics, and energy conversion efficiency.[17,18] In order to further improve the intrinsic electrocatalytic capability of TMSes, there are some recent reports on construction of heterostructures to adjust the interface electronic structures, such as $NiSe_2$–$NiFe_2Se_4$, Ni_2P–$NiSe_2$, $NiSe_2$–$CoSe_2$, *etc.*[19–21] By constructing heterostructures, the charge transfer efficiency within the catalyst can be significantly enhanced due to the electricity differences of the two phases, while new active sites with a moderately regulated electronic structure that adapts for the adsorption of reaction intermediates generate at the heterogeneous phase boundaries.[22–24] To maximally expose those highly active sites in TMSe-based heterostructures, different morphological regulation strategies have been proposed, such as designing ultra-thin nanosheets or nickel foam-based

State Key Laboratory of Heavy Oil Processing, China University of Petroleum, Changping, Beijing 102249, China. E-mail: yangfan@cup.edu.cn, yfli@cup.edu.cn

† Electronic supplementary information (ESI) available. See DOI: https://doi.org/10.1039/d2qm01082h

nanoarrays.[25,26] However, the electrochemical active surface area and the amount of mass transfer paths of these structures still remain to be improved. Recently, metal aerogels have been widely researched due to their unique properties between powders and self-supporting materials. Compared with other powder materials, metal aerogels have three-dimensional interconnected network structures without carriers, which not only present a high specific area with plenty of active sites, but also provide abundant pathways for mass transfer.[27,28] Benefiting from the advantages of the aerogel structure, some transition-metal-based structures have been reported as high-performance water electrolysis catalysts.[29,30] For example, we have designed and prepared a P, Mo-codoped Ni aerogel (Ni–Mo–P aerogel) for electrocatalytic overall water splitting in our previous work. In contrast to the nanowires with the same composition, the Ni–Mo–P aerogel exhibits a larger electrochemical surface area and a better HER performance.[31] Nevertheless, there are few reports dedicated to combining the TMSes or TMSe-based heterostructures and the unique aerogel morphology for efficient overall water splitting.

In this work, a $NiSe_2$–$CoSe_2$ aerogel was prepared by spontaneous gelation and selenium vapor deposition. The bifunctional $NiSe_2$–$CoSe_2$ catalyst exhibited an impressive performance for the HER (65 mV@10 mA cm^{-2}) and the OER (220 mV@10 mA cm^{-2}), and the assembled symmetrical overall water splitting system required a low cell voltage of 1.56 V to achieve a current density of 10 mA cm^{-2}. The eminent performance of the optimized sample was attributed to the following two aspects: (1) the heterogeneous structure constructed by $NiSe_2$ and $CoSe_2$ led to the generation of active sites with ideal adsorption capability for reactant intermediates at the interface. Meanwhile, the charge transfer efficiency of the material was significantly improved due to the electrical property contrast of the two phases. (2) The $NiSe_2$–$CoSe_2$ heterostructure with higher intrinsic activity was successfully prepared with an aerogel morphology, providing a high specific surface area with lots of exposed active sites. This work provides a new perspective for the design of TMSe-based electrocatalysts for overall water splitting.

Materials and methods

Materials and reagents

Nickle chloride hexahydrate ($NiCl_2{\cdot}6H_2O$, AR) and cobalt chloride hexahydrate ($CoCl_2{\cdot}6H_2O$, AR) were purchased from Sinopharm Chemical Reagent Co. Sodium borohydride ($NaBH_4$, 98%) was purchased from TianJin Fuchen Chemical Reagents Factory. Selenium (Se, 99.99%, powder, 100) was purchased from Adamas-beta. Pt/C (20 wt%) and RuO_2 were purchased from Alfa Aesar.

Ni–Co aerogel synthesis

In a typical preparation of the Ni–Co aerogel, 15 mL of $NaBH_4$ (0.1 M) solution was quickly dropped into the mixed solution of 10 mL Ni^{2+} (0.05 M) and Co^{2+} (0.05 M). After 8 hours of gelation, the Ni–Co hydrogel was formed at the bottom of the flask. After 20 h of freeze drying, moisture was removed and the Ni–Co aerogel (Ni–Co-1 : 1) was obtained. As comparison samples, the molar ratio of Ni^{2+} and Co^{2+} was changed to 2 : 1, 1 : 2, 1 : 0 and 0 : 1 to prepare the Ni–Co-2 : 1, Ni–Co-1 : 2, pure Ni and Co aerogels, respectively.

$NiSe_2$–$CoSe_2$ aerogel synthesis

To fabricate the $NiSe_2$–$CoSe_2$ aerogel, 20 mg of the Ni–Co-1 : 1 aerogel and excess Se powder were placed at two separate positions in porcelain boats, respectively, of which Se powder was placed on the upstream side of the furnace. Then, the samples were heated up to 400 °C at 5 °C min^{-1} and maintained at this temperature for 120 min with Ar gas flowing at 50 sccm to obtain the $NiSe_2$–$CoSe_2$ aerogel. The comparison samples prepared in the previous step were selenized in the same way to get $NiSe_2$–$CoSe_2$-2 : 1, $NiSe_2$–$CoSe_2$-1 : 2, $NiSe_2$ and $CoSe_2$ aerogels, respectively. To investigate the influence of selenide temperature and determine the best reaction conditions, $NiSe_2$–$CoSe_2$-300 and $NiSe_2$–$CoSe_2$-500 aerogels were prepared by changing the reaction temperature to 300 °C and 500 °C, respectively.

Materials characterization

Scanning electron microscopy (SEM) measurements were performed on a SU8010 microscope at an accelerating voltage of 5 kV. Transmission electron microscopy (TEM) and energy disperse spectroscopy (EDS) images were recorded using a Tecnai G2 F20 field emission transmission electron microscope. Inductively coupled plasma-optical emission spectroscopy (ICP-OES) results were obtained from an Agilent ICPOES 730. Powder X-ray diffraction (XRD) was studied using a Bruker D8 Advance diffractometer. X-ray photoelectron spectroscopy (XPS) data of the samples were recorded on a Thermo Fisher K-Alpha American with an Al K X-ray source.

Electrochemical measurements

Samples on carbon-cloth-based electrodes were prepared for all the electrochemical measurements. In this context, 5.0 mg of the sample was dispersed in the mixed solution with 0.25 mL ethanol and 0.25 mL deionized water, containing 20 μL of Nafion (5%) under sonication for 30 min to form a homogeneous catalyst ink. Then, the obtained ink was drop-cast onto the surface of carbon cloth (1 cm × 1 cm) followed by drying at 60 °C for 5 h to achieve the loading amount of 1.0 mg cm^{-2} for the sample on carbon cloth. For a comparison, Pt/C and RuO_2 on carbon cloth were also prepared for evaluating HER, OER and overall water splitting by the same method.

All the electrochemical properties of the samples were measured on a CHI 760 electrochemical workstation (CH Instruments, Inc., Shanghai) integrated with a three-electrode system at room temperature. Sample modified carbon cloth, graphite rod, and Hg/HgO acted as working, counter, and reference electrodes, respectively. The conversion potential of E (RHE) was obtained according to the following equation:

$$E(\mathrm{RHE}) = E(\mathrm{Hg/HgO}) + 0.059 \times \mathrm{pH} + 0.098$$

Electrocatalytic performance of the HER and OER were tested by linear-sweep voltammetry in 1 M KOH solution at a

scan rate of 5 mV s^{-1}. The potential range of the HER and OER was −0.8 to −1.4 V and 0 to 0.8 V *vs.* the standard Hg/HgO electrode, respectively. All the polarization curves of the HER and OER were adjusted with 90% IR-correction according to the ohmic resistance of the solution (R_s), and the values of R_s was obtained from the electrochemical impedance spectroscopy (EIS) results under the open circuit potential. Besides, electrocatalytic performance of overall water splitting were tested by LSV on an electrolytic cell consisting of two carbon cloth electrodes with the optimized sample under the operating voltage from 1.0 to 2.0 V (without IR-correction). EIS measurements were applied to evaluate the charge transfer ability of the catalysts at a frequency range of 0.01 to 10^5 Hz under the voltage of −1.1 V. Double-layer capacitance (C_{dl}) values were assessed by cyclic voltammetry (CV) in the non-faradaic potential region ranging from −0.3 to −0.5 V *vs.* standard Hg/HgO electrode at 10 mV s^{-1}, 50 mV s^{-1}, 100 mV s^{-1}, 150 mV s^{-1}, and 200 mV s^{-1}. Stability of samples was tested by chronoamperometric measurement under the voltages to achieve a current density of 10 mA cm^{-2}.

Theoretical calculations

Density functional theory (DFT) calculation was performed using the DMol^3 code as implemented in Materials Studio. The generalized gradient approximation of the Perdew–Burke–Ernzerhof (GGA-PBE) function was used to treat all the energy changes. The core treatment was effective core potentials (ECP) and the basis set was DNP v4.4. The *k*-point was set as 3 × 3 × 1 and the size of vacuum region was 15 Å. The Ni–Co model was formed by Ni(111) and Co(111) layers, and $NiSe_2$, $CoSe_2$, $NiSe_2$–$CoSe_2$ models were formed by $NiSe_2$(210) and $CoSe_2$(210) layers. The typical Ni–Co surface was modified by the $U \times 2$ and $V \times 2$ super cell of the Ni(111)–Co(111) layer, while all the selenide surfaces were modified by the $U \times 2$ and $V \times 1$ super cell of corresponding $NiSe_2$(210), $CoSe_2$(210) or $NiSe_2$(210)–$CoSe_2$(210) layers. The adsorption energies of hydrogen atoms and reaction intermediates of the OER on the structures were calculated by the following equation:

$$\Delta G = \Delta E + \Delta ZPE - T\Delta S$$

In the equation, the ΔZPE and Δ*S* in the formula are the zero-point energy change and the entropy change between the surface and the adsorbed reaction intermediate molecule, which were obtained from the frequency calculation function of the DMol^3 code. *T* was the temperature of the system, which was set to 298.15 K in all the calculations. Besides the Δ*E* was the binding energy of reaction intermediates and could be calculated by the following equation:

$$\Delta E = E_{(surf+i)} - E_{(surf)} - E_i$$

Herein, the $E_{(surf)}$ and E_i represented the energies of the bare surface and reaction intermediates (H* in the HER and OH*, O*, and OOH* in the OER), respectively. The $E_{(surf+i)}$ was the total energy of the obtained surface structure with an adsorbed reaction intermediate molecule.

Results and discussion

Catalyst synthesis and characterizations

The synthetic procedure of the $NiSe_2$–$CoSe_2$ aerogel involved three facile steps (Fig. 1). First of all, the Ni–Co hydrogel was synthesized *via* the spontaneous $NaBH_4$ reduction and gelation process. The corresponding reactions of this step was described by the following equations:

$$Ni^{2+} + NaBH_4 + 2H_2O \rightarrow Ni + NaBO_2 + 2H^+ + 2H_2$$

$$Co^{2+} + NaBH_4 + 2H_2O \rightarrow Co + NaBO_2 + 2H^+ + 2H_2$$

$$NaBH_4 + 2H_2O \rightarrow NaBO_2 + 4H_2$$

During this step, the *in situ* generated H_2 gas from the reduction of Ni, Co elements and the hydrolysis of $NaBH_4$ served as the gas template, directing the formation of porous interconnected networks (Fig. S1, ESI†).[31,32] Then, the corresponding aerogel was obtained by freeze-drying without damaging the morphology of the gel. Finally, the Ni–Co aerogel was annealed under a selenium vapor atmosphere to obtain the $NiSe_2$–$CoSe_2$ aerogel.

The morphologies and structures of the $NiSe_2$–$CoSe_2$ aerogel were characterized by SEM. To be specific, the Ni–Co precursor and $NiSe_2$–$CoSe_2$ aerogel exhibited the fluffy overall morphology in the large-scale images (Fig. S2(a) and (b), ESI†). Moreover, the Ni–Co aerogel presented a three-dimensional interconnected network formed by bimetallic alloy nanoparticles (Fig. 2(a)). After selenization, the $NiSe_2$–$CoSe_2$ aerogel still maintained the unique porous morphology (Fig. 2(b)), which could be further confirmed by the high-resolution SEM images (Fig. S2(c) and (d), ESI†) and low-resolution TEM images (Fig. S3, ESI†). Such a shaggy and porous structure provided abundant active sites and mass transfer pathways.[32,33] According to reported literatures and our previous works,[28,31,34] the type and mole ratio of metals are the key factors affecting the morphology of the aerogel. Notably, the $NiSe_2$–$CoSe_2$-2 : 1 and $NiSe_2$ aerogels with a higher Ni content tended to form the network structure composed of comparatively small nanoparticles (Fig. S4(a) and (c), ESI†), while the $NiSe_2$–$CoSe_2$-1 : 2 and $CoSe_2$ were entirely comprised of larger nanoparticles without an appreciable network skeleton (Fig. S4(b) and (d), ESI†).[35] In addition, the selenization temperature also played an important role in modulating the

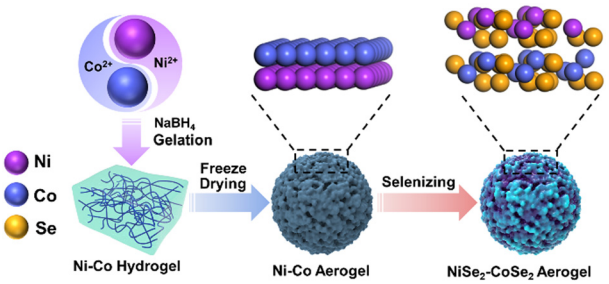

Fig. 1 Schematic illustration of the synthesis of Ni–Co and $NiSe_2$–$CoSe_2$ aerogels.

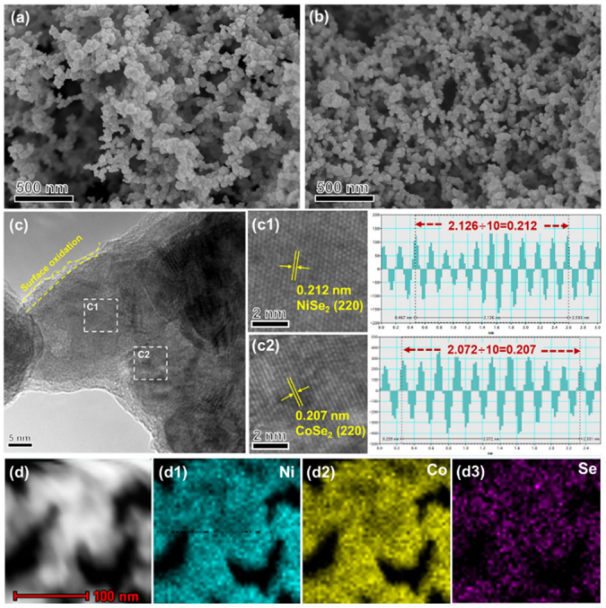

Fig. 2 (a and b) SEM images of the Ni–Co and $NiSe_2$–$CoSe_2$ aerogel. (c) HRTEM image of the $NiSe_2$–$CoSe_2$ aerogel with lattice fringes of $NiSe_2$ and $CoSe_2$ (c1 and c2). (d) STEM image of the $NiSe_2$–$CoSe_2$ aerogel and its corresponding EDX mapping of Ni, Co, Se (d1–d3).

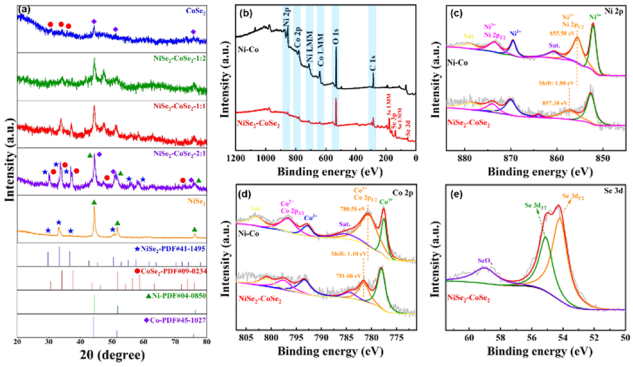

Fig. 3 (a) XRD patterns of the $NiSe_2$–$CoSe_2$ aerogel and comparison samples. (b) XPS survey spectrum of Ni–Co and $NiSe_2$–$CoSe_2$ aerogels. (c and d) High resolution Ni 2p and Co 2p XPS spectra of Ni–Co and $NiSe_2$–$CoSe_2$ aerogels. (e) High resolution Se 3d XPS spectra of the $NiSe_2$–$CoSe_2$ aerogel.

morphology. $NiSe_2$–$CoSe_2$-300 was identified to retain the porous network structure, while $NiSe_2$–$CoSe_2$-500 agglomerated obviously and gradually lost the aerogel morphology (Fig. S5, ESI†). The HRTEM of the $NiSe_2$–$CoSe_2$ aerogel is shown in Fig. 2(c). Because of contact with air, a thick oxide layer was formed on the surface of aerogel.[34,36] Based on the results of Fast Fourier Transform (FFT), the (220) crystal planes of $NiSe_2$ (0.212 nm, Fig. 2(c1)) and $CoSe_2$ (0.207 nm, Fig. 2(c2)) were observed, which preliminarily proved the formation of the $NiSe_2$–$CoSe_2$ heterostructure.[21,26] Besides, the STEM-mapping of the $NiSe_2$–$CoSe_2$ aerogel showed that Ni, Co, and Se were evenly distributed in the skeleton (Fig. 2(d1)–(d3)), which revealed the construction of the selenide aerogel. Meanwhile, the Ni, Co, and Se contents of $NiSe_2$–$CoSe_2$, $NiSe_2$–$CoSe_2$-2 : 1 and $NiSe_2$–$CoSe_2$-1 : 2 were analyzed by SEM-EDS (Fig. S6, ESI†) and further confirmed by the results of ICP-OES (Table S1, ESI†). The proportion of Ni and Co in each sample conformed well to our design, while the Se contents were 30–40 wt%.

The crystalline structure of $NiSe_2$–$CoSe_2$ and comparison samples were investigated by XRD (Fig. 3(a)). The patterns of $NiSe_2$–$CoSe_2$-1 : 1, $NiSe_2$–$CoSe_2$-2 : 1 and $NiSe_2$–$CoSe_2$-1 : 2 aerogels exhibited the characteristic diffraction peaks of $NiSe_2$ (PDF#41-1495) and $CoSe_2$ (PDF#09-0234). Meanwhile, the selenides on the surface of the aerogel prevented selenium vapor from contacting the Ni and Co inside the skeleton, so that the corresponding peaks of Ni (PDF#04-0850) and Co (PDF#45-1027) could be observed in the patterns.[19] Compared with the standard cards, the shift and superposition of $NiSe_2$ and $CoSe_2$ characteristic peaks at 30°–40° could be observed, which was attributed to the lattice distortion caused by the interaction between the two selenide crystals, thus proving the formation of a bimetallic selenide heterostructure.[37,38]

In addition, the $NiSe_2$ aerogel showed good crystallinity with distinct characteristic peaks of Ni and $NiSe_2$, but the crystallinity of the $CoSe_2$ aerogel was comparatively poor due to the easy formation of an amorphous oxide layer on the surface.[39,40] Therefore, the crystallization degree of the aerogels could be regulated by constructing a bimetallic selenide heterostructure to expose highly-active crystal planes.[41]

XPS analysis was used to analyze the chemical states of Ni–Co and $NiSe_2$–$CoSe_2$ aerogels. As demonstrated in Fig. 3(b), the survey spectrum of Ni–Co and $NiSe_2$–$CoSe_2$ aerogels demonstrated the co-presence of Ni, Co, C, and O fundamental elements. The characteristic peak of Se 3d was observed for the $NiSe_2$–$CoSe_2$ aerogel, which indicated the generation of selenides. The high-resolution Ni 2p and Co 2p spectra were respectively manifested in Fig. 3(c) and (d), and four major peaks of Ni and Co with two satellite peaks were identified. For the Ni–Co aerogel, the peaks located at 852.1 and 869.5 eV were assigned to Ni^{3+}, and the peaks at 855.5 and 873.4 eV were attributed to Ni^{2+} of Ni $2p_{3/2}$ and Ni^{2+} of Ni $2p_{1/2}$, respectively. Similarly, the peaks located at 777.5 and 792.8 eV were fitted to Co^{3+}, and the peaks at 780.5 and 796.6 eV were assigned to the Co^{2+} $2p_{3/2}$ and Co $^{2+}$ of Co $2p_{1/2}$, respectively.[21] For $NiSe_2$–$CoSe_2$, the peaks of Ni^{2+} and Co^{2+} showed obvious positive shifts of 1.80 eV and 1.10 eV, respectively, indicating the electronic structure regulation due to selenization. Such alteration of electron densities around the bimetallic atoms could benefit the adsorption of OH^- ions and the desorption of H* during alkaline electrocatalytic water splitting.[42] Fig. 3(e) showed the Se 3d spectra of the $NiSe_2$–$CoSe_2$ aerogel. The peaks at 54.2 and 55.1 eV were assigned to Se^{2-} of Se $3d_{5/2}$ and Se^{2-} of Se $3d_{3/2}$, while the peak at 59.0 eV was attributed to SeO_x due to air oxidation.[43]

Electrocatalytic activity toward the HER

The electrocatalytic activity of $NiSe_2$–$CoSe_2$ toward the HER was investigated through LSV in 1.0 M KOH under a scan rate of 5 mV s^{-1}. For comparison, $NiSe_2$, $CoSe_2$, Ni–Co aerogels, and commercial Pt/C on carbon cloth with similar mass loading

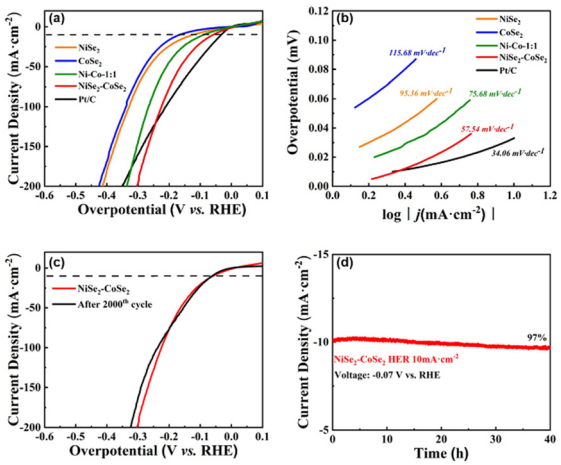

Fig. 4 (a and b) Polarization LSV curves and Tafel slopes of $NiSe_2$, $CoSe_2$, Ni–Co, and $NiSe_2$–$CoSe_2$ aerogels and Pt/C toward the HER in 1.0 M KOH. (c) Cyclic stability of $NiSe_2$–$CoSe_2$ toward the HER. (d) Chronoamperometric measurement of $NiSe_2$–$CoSe_2$ toward the HER.

were also tested (Fig. 4(a), and the curves before IR-correction are shown in Fig. S7, ESI†). The Pt/C showed the lowest overpotential of 34 mV@10 mA cm^{-2}, which was consistent with the reported literature.[44] The $NiSe_2$–$CoSe_2$ also afforded remarkable HER activity with an overpotential of only 65 mV@10 mA cm^{-2}. It obviously outperformed the counterparts of the $NiSe_2$ aerogel (131 mV@10 mA cm^{-2}), $CoSe_2$ aerogel (173 mV@10 mA cm^{-2}), and Ni–Co aerogel (94 mV@10 mA cm^{-2}), indicating the synergic enhancement of the bimetallic selenide heterostructure. In order to determine the best ratio of Ni and Co, we also tested the HER performance of $NiSe_2$–$CoSe_2$-2 : 1 (84 mV@10 mA cm^{-2}) and $NiSe_2$–$CoSe_2$-1 : 2 aerogels (92 mV@10 mA cm^{-2}) (Fig. S8(a) (ESI†), and the curves before IR-correction are shown in Fig. S8(b), ESI†). It was found that the sample with the balanced ratio of Ni and Co (1 : 1) showed the best performance, indicating the optimized construction of a heterogeneous interface under this ratio. To optimize the selenization temperature, we tested the HER performance of $NiSe_2$–$CoSe_2$-300 (95 mV@10 mA cm^{-2}) and $NiSe_2$–$CoSe_2$-500 (133 mV@10 mA cm^{-2}) as well (Fig. S8(c), ESI,† and the curves before IR-correction are shown in Fig. S8(d), ESI†). $NiSe_2$–$CoSe_2$-300 showed similar HER performance with the Ni–Co aerogel, indicating that $NiSe_2$–$CoSe_2$-300 was barely selenized at 300 °C. Meanwhile, the performance of $NiSe_2$–$CoSe_2$-500 decreased significantly due to structural agglomeration under the elevated temperature of 500 °C. Thus, we determined that 400 °C was the optimized selenization temperature. Tafel plots were further conducted to analyze the electrocatalytic performance. In Fig. 4(b), the $NiSe_2$–$CoSe_2$ aerogel delivered a Tafel slope of 57.54 mV dec^{-1}, lower than those of $NiSe_2$ (95.36 mV dec^{-1}), $CoSe_2$ (115.68 mV dec^{-1}), and Ni–Co (75.68 mV dec^{-1}) aerogels. The low Tafel slope on the $NiSe_2$–$CoSe_2$ aerogel indicated the accelerated H_2 generation with the applied overpotential, in accordance with its high activity.[3] Tafel slopes of aerogels with different metal proportions and different selenization temperatures were also calculated in Fig. S9 (ESI†), which were also consistent with their HER performances. The cyclic stability of the $NiSe_2$–$CoSe_2$ aerogel with the best performance was tested by cyclic voltammetry and chronoamperometric measurement at an initial current density of 10 mA cm^{-2} (Fig. 4(c) and (d)). A tiny deflection of LSV results was observed before and after 2000 CV cycles, verifying the impressive stability of the $NiSe_2$–$CoSe_2$ aerogel. After a 40 h test, the current density retained 97% of the initial value, which further indicated the favorable stability of the $NiSe_2$–$CoSe_2$ aerogel.

Electrocatalytic activity towards OER and overall water splitting

The OER polarization curve of the $NiSe_2$–$CoSe_2$ aerogel and contrast samples were also determined through LSV in 1.0 M KOH under a scan rate of 5 mV s^{-1} (Fig. 5(a), and the curves before IR-correction are shown in Fig. S10, ESI†). The oxidation peaks could be observed at around 1.33 V in the curves of $NiSe_2$ and $CoSe_2$ aerogels, which represented the reconstruction process and the generation of OOH*.[42] In contrast with the single metallic selenides, the Ni–Co aerogel exhibited a lower onset voltage of oxidation at 1.25 V, indicating that the facilitated charge transfer efficiency enhanced the reconstruction process. As Ni–Co was further selenized to $NiSe_2$–$CoSe_2$, the onset voltage of oxidation decreased to 1.23 V, demonstrating that the bimetallic selenide heterostructure had the surface that favored to reconstruct and generate active sites with excellent OER performance.[10] Benefiting from the rapid reconstruction, $NiSe_2$–$CoSe_2$ exhibited the lowest overpotential of 220 mV@10 mA cm^{-2}, significantly better than that of $NiSe_2$ (304 mV), $CoSe_2$ (289 mV) and Ni–Co (265 mV). Notably, the performance of the $NiSe_2$–$CoSe_2$ aerogel was superior to the commercial RuO_2 (251 mV@10 mA cm^{-2}), demonstrating that the selenide heterostructure possessed great application potential in the electrocatalytic OER process. Besides, $NiSe_2$–$CoSe_2$ exhibited a Tafel slope of 99.57 mV dec^{-1}, lower than that of $NiSe_2$ (157.71 mV dec^{-1}), $CoSe_2$ (131.52 mV dec^{-1}) and Ni–Co (109.47 mV dec^{-1}), which indicated the favorable reaction kinetics of the Ni–Co selenide heterostructure (Fig. 5(b)).

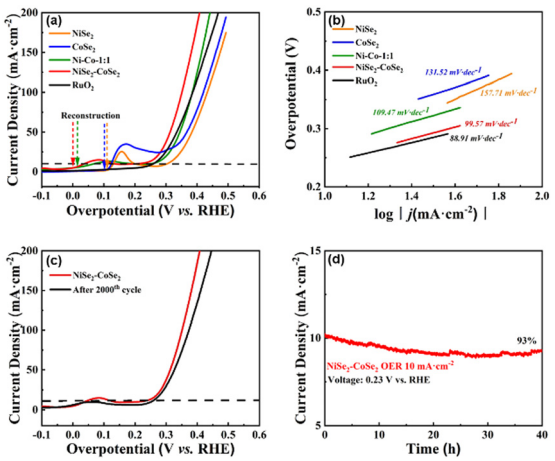

Fig. 5 (a and b) Polarization LSV curves and Tafel slopes of $NiSe_2$–$CoSe_2$, $NiSe_2$ and $CoSe_2$ aerogels and RuO_2 toward the OER in 1.0 M KOH. (c) Cyclic stability of $NiSe_2$–$CoSe_2$ toward the OER. (d) Chronoamperometric measurement of $NiSe_2$–$CoSe_2$ toward the OER.

To further illustrate the optimal metal ratio and reaction temperature, the OER properties of $NiSe_2$–$CoSe_2$-2 : 1, $NiSe_2$–$CoSe_2$-1 : 2, $NiSe_2$–$CoSe_2$-300, and $NiSe_2$–$CoSe_2$-500 aerogels were also tested (Fig. S11 and S12, ESI†). Similar to the HER, the sample with a metal ratio of 1 : 1 and selenization temperature of 400 °C had the best OER performance. All of the above results indicated that the optimized $NiSe_2$–$CoSe_2$ had the best OER performance due to its balanced ratio of $NiSe_2$/$CoSe_2$ and favorable morphology. Stability of $NiSe_2$–$CoSe_2$ toward the OER was also evaluated by cyclic voltammetry and chronoamperometric measurements at an initial current density of 10 mA cm^{-2} (Fig. 5(c) and (d)). A deflection of LSV results was observed before and after 2000 CV cycles. Such a change in performance mainly came from the sample falling out caused by oxygen bubble overflow. After a 40 h test, 93% of the initial value of the current density was retained, indicating the favorable stability of the $NiSe_2$–$CoSe_2$ aerogel toward the OER.

In another regard, the excellent performance of $NiSe_2$–$CoSe_2$ toward both the HER and OER in an alkaline medium could also be accounted for the high charge transfer efficiency and large electrochemically active surface area (ECSA)-introduced efficient charge transfer and abundant active sites. The charge transfer resistances (R_{ct}) of $NiSe_2$–$CoSe_2$ and comparison samples were tested by EIS analysis (Fig. 6(a)). Compared with $NiSe_2$ (39.70 Ω), $CoSe_2$ (59.51 Ω), and Ni–Co (25.87 Ω) aerogels, the $NiSe_2$–$CoSe_2$ showed the lowest R_{ct} of 12.16 Ω, indicating the enhanced charge transfer ability offered by the heterostructure. Besides, we also tested the conductivities of other prepared samples (Fig. S13, ESI†). $NiSe_2$–$CoSe_2$ showed the best electron conductive performance, which further supported the optimal preparation conditions. After that, electrochemical double-layer capacitance (C_{dl}) was applied to estimate the electrochemical surface area of different samples (Fig. 6(b)) based on CV curves (Fig. S14, ESI†). The C_{dl} value of the $NiSe_2$–$CoSe_2$ aerogel was calculated to be 18.50 mF cm^{-2}, which was higher than that of $NiSe_2$ (3.64 mF cm^{-2}), $CoSe_2$ (3.25 mF cm^{-2}), and Ni–Co (1.16 mF cm^{-2}) aerogels, indicating that the heterostructure activated additional exposed active sites. The same electrochemical tests were performed on other comparison samples (Fig. S15, ESI†), and the $NiSe_2$–$CoSe_2$ aerogel exhibited a higher C_{dl} value than other aerogels, suggesting that the sufficient construction of the heterostructure based on the optimal preparation conditions could fully activate catalytic sites and provide a large electrochemical surface area. Besides, the optimized $NiSe_2$–$CoSe_2$ aerogel exhibited a C_{dl} value superior to some reported selenides or heterostructure electrocatalysts with other nanostructures (Table S2, ESI†), proving plenty of active sites and abundant mass transfer pathways provided by the aerogel skeleton.

On the basis of good activities of HER and OER, an overall water splitting cell was prepared with two $NiSe_2$–$CoSe_2$ electrodes under alkaline conditions (Fig. 6(c)). The $NiSe_2$–$CoSe_2$ aerogel device exhibited a low potential of 1.56 V@10 mA cm^{-2}, which was equal to the performance of Pt/C + RuO_2 (1.56 V). Note that the ratio of H_2 and O_2 was close to 2 : 1 (Fig. S16, ESI†), indicating that the faradaic efficiency (FE) was nearly 100% for each gas evolution reaction.[21] Besides, the activity of $NiSe_2$–$CoSe_2$ was also comparable with other reported selenides or heterostructure electrocatalysts (Table S3, ESI†). In addition to catalytic activity, the stability of the overall water splitting cell was also investigated. Fig. 6(d) shows that the $NiSe_2$–$CoSe_2$ device had decent durability, with a current retention of 91% after 40 h operation. Furthermore, the XRD patterns of $NiSe_2$–$CoSe_2$ after the stability test of overall water splitting are shown in Fig. S17 (ESI†). The characteristic peaks of selenides ($NiSe_2$ and $CoSe_2$) and metal elements (Ni and Co) that are identical to the unreacted sample could be observed in the XRD pattern of the cathodic $NiSe_2$–$CoSe_2$ aerogel, suggesting that the overall structure and composition of the tested hybrid was unaltered. This result could indicate the superior electrochemical stability of the selenides heterostructure in the HER process.[21] Moreover, there were no obvious peaks in the XRD pattern of the anodic $NiSe_2$–$CoSe_2$ aerogel, which was attributed to the transformation of crystal structures from selenides and metal elements to reconstructed hydroxides ($Ni(OH)_2$ and $Co(OH)_2$) and hydroxyl oxides (NiOOH and CoOOH) in the OER process.[42]

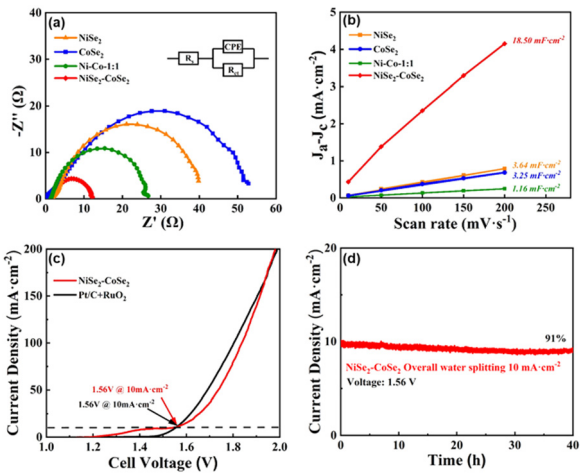

Fig. 6 (a) EIS measurements of prepared samples. (b) C_{dl} values of prepared samples. (c) LSV measurements for overall water splitting performance of the devices based on $NiSe_2$–$CoSe_2$ electrodes and Pt/C + RuO_2 electrodes. (d) Chronoamperometric measurement of $NiSe_2$–$CoSe_2$ aerogel toward overall water splitting.

Theorical calculation

To further understand the origin of the observed excellent performance of both the HER and OER on the $NiSe_2$–$CoSe_2$ aerogel, theoretical calculations were conducted using density functional theory (DFT) with the Materials Studio-DMol.[3] Considering the complexity of the aerogel with surface oxidation and metals without selenide, we simplified the model and focused on the interactions within the bimetallic selenide heterostructure. Based on the XRD results, we formed the models of Ni–Co, $NiSe_2$, $CoSe_2$, and $NiSe_2$–$CoSe_2$, and all structures are shown in Fig. 7(a). For the HER process, we mainly focused on the adsorption properties of metal sites (Ni or Co site) for H* (Fig. 7(b)). In the $NiSe_2$–$CoSe_2$ structure, the Ni site exhibited stronger free energy of hydrogen adsorption (ΔG_{H^*}, −0.26 eV) than that of the Co site

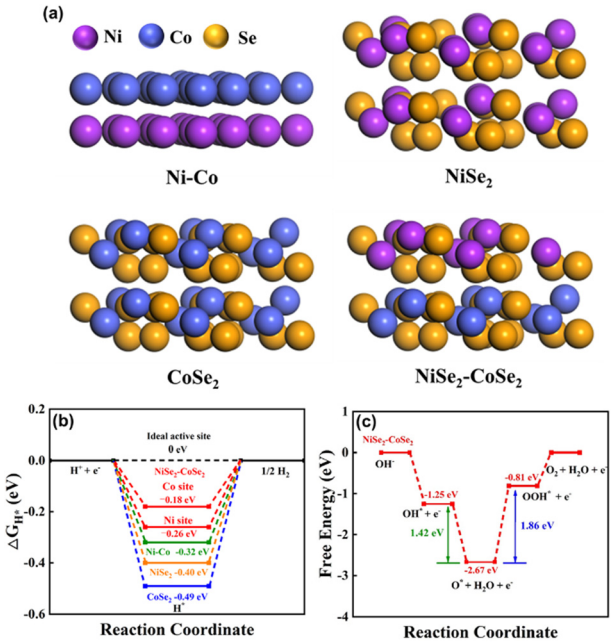

Fig. 7 (a) Crystal models of Ni–Co, $NiSe_2$, $CoSe_2$, and $NiSe_2$–$CoSe_2$ constructed based on the XRD. (b) Free energy diagram of the HER for different catalysts. (c) Free energy diagram of the OER for $NiSe_2$–$CoSe_2$.

(−0.18 eV), indicating that electrons transferred from $CoSe_2$ to $NiSe_2$ at the heterointerface. In contrast, the Co site had the ΔG_{H^*} closer to zero (ideal state), demonstrating the favorable adsorption properties and high activity toward the HER. Meanwhile, the Co site in $NiSe_2$–$CoSe_2$ had markedly better adsorption properties toward H* than that of Ni–Co (−0.32 eV), $NiSe_2$ (−0.40 eV) and $CoSe_2$ (−0.49 eV), indicating the superior activity toward the HER on the heterointerface between $NiSe_2$ and $CoSe_2$.[21] Furthermore, we proposed the detailed OER mechanism of $NiSe_2$–$CoSe_2$ by DFT calculations. The OER reaction could be divided into the following 4 steps:

$$M + OH^- = M{\cdot}OH^* + e^-$$

$$M{\cdot}OH^* + OH^- = M{\cdot}O^* + H_2O + e^-$$

$$M{\cdot}O^* + OH^- = M{\cdot}OOH^* + e^-$$

$$M{\cdot}OOH^* + OH^- = M + O_2 + H_2O + e^-$$

The calculated results (Fig. 7(c)) showed that the third electron transfer step to form *OOH exhibited the largest ladder span with an energy barrier of 1.86 eV, which was the rate-limiting step of the OER.[45] Besides, the free energy difference between the intermediates HO* and OOH* was a definite value (about 3.2 eV). When the difference of the energy barriers between HO* to O* and O* to OOH* was smaller, the OER process would be easier.[46] For the $NiSe_2$–$CoSe_2$, the difference value between the two steps was only 0.43 eV, which further validated the excellent reaction kinetics. All the theoretical calculations were in good agreement with the experimental results.

Conclusions

In summary, we designed and synthesized a $NiSe_2$–$CoSe_2$ aerogel *via* spontaneous gelation followed by a facile chemical vapor deposition selenide process. The bifunctional $NiSe_2$–$CoSe_2$ aerogel showed splendid HER, OER and overall water splitting capabilities with low potentials and favorable stabilities. Systematic characterization, electrochemical testing and DFT calculations illustrated that the superior performances were attributed to the large effective surface area of the aerogel with a three-dimensional interconnected network structure, as well as the high intrinsic activity of the heterostructure formed by $NiSe_2$ and $CoSe_2$. Our work afforded an uncomplicated approach to construct potentially scalable electrocatalysts using TMSe-based aerogels.

Conflicts of interest

There are no conflicts to declare.

Acknowledgements

The authors gratefully thank the National Natural Science Foundation of China (No. 22278431 and No. 21776302) and the Science Foundation of China University of Petroleum, Beijing (No. 2462020YXZZ033) for financial support of this work.

Notes and references

1 I. Staffell, D. Scamman, A. Velazquez Abad, P. Balcombe, P. E. Dodds, P. Ekins, N. Shah and K. R. Ward, The role of hydrogen and fuel cells in the global energy system, *Energy Environ. Sci.*, 2019, **12**, 463–491.
2 J. Schmidt, K. Gruber, M. Klingler, C. Klöckl, L. Ramirez Camargo, P. Regner, O. Turkovska, S. Wehrle and E. Wetterlund, A new perspective on global renewable energy systems: Why trade in energy carriers matters, *Energy Environ. Sci.*, 2019, **12**, 2022–2029.
3 J. Zhu, L. Hu, P. Zhao, L. Y. S. Lee and K. Y. Wong, Recent Advances in Electrocatalytic Hydrogen Evolution Using Nanoparticles, *Chem. Rev.*, 2020, **120**, 851–918.
4 E. Fabbri, A. Habereder, K. Waltar, R. Kötz and T. J. Schmidt, Developments and perspectives of oxide-based catalysts for the oxygen evolution reaction, *Catal. Sci. Technol.*, 2014, **4**, 3800–3821.
5 J. Greeley, T. F. Jaramillo, J. Bonde, I. Chorkendorff and J. K. Nørskov, Computational high-throughput screening of electrocatalytic materials for hydrogen evolution, *Nat. Mater.*, 2006, **5**, 909–913.
6 M. Chen, D. Liu, B. Zi, Y. Chen, D. Liu, X. Du, F. Li, P. Zhou, Y. Ke, J. Li, K. H. Lo, C. T. Kwok, W. F. Ip, S. Chen, S. Wang, Q. Liu and H. Pan, Remarkable synergistic effect in cobalt-iron nitride/alloy nanosheets for robust electrochemical water splitting, *J. Energy Chem.*, 2021, **65**, 405–414.
7 Y. Zhou, B. Tang, S. Wang and J. Long, Cu-MOF@Co-MOF derived Co–Cu alloy nanoparticles and N atoms co-doped

carbon matrix as efficient catalyst for enhanced oxygen reduction, *Int. J. Hydrogen Energy*, 2020, **45**, 15785–15795.
8 A. Parra-Puerto, K. L. Ng, K. Fahy, A. E. Goode, M. P. Ryan and A. Kucernak, Supported Transition Metal Phosphides: Activity Survey for HER, ORR, OER, and Corrosion Resistance in Acid and Alkaline Electrolytes, *ACS Catal.*, 2019, **9**, 11515–11529.
9 Y. Zhao, S. Wei, K. Pan, Z. Dong, B. Zhang, H. H. Wu, Q. Zhang, J. Lin and H. Pang, Self-supporting transition metal chalcogenides on metal substrates for catalytic water splitting, *Chem. Eng. J.*, 2021, **421**, 129645.
10 X. Peng, Y. Yan, X. Jin, C. Huang, W. Jin, B. Gao and P. K. Chu, Recent advance and prospectives of electrocatalysts based on transition metal selenides for efficient water splitting, *Nano Energy*, 2020, **78**, 105234.
11 M. S. Balogun, Y. Huang, W. Qiu, H. Yang, H. Ji and Y. Tong, Updates on the development of nanostructured transition metal nitrides for electrochemical energy storage and water splitting, *Mater. Today*, 2017, **20**, 425–451.
12 I. Concina, Z. H. Ibupoto and A. Vomiero, Semiconducting metal oxide nanostructures for water splitting and photovoltaics, *Adv. Energy Mater.*, 2017, **7**, 1–29.
13 J. Mohammed-ibrahim and H. Moussab, Tuning the electronic structure of the earth-abundant electrocatalysts for oxygen evolution reaction (OER) to achieve efficient alkaline water splitting – A review, *J. Energy Chem.*, 2021, **56**, 299–342.
14 S. Anantharaj, S. R. Ede, K. Sakthikumar, K. Karthick, S. Mishra and S. Kundu, Recent Trends and Perspectives in Electrochemical Water Splitting with an Emphasis on Sulfide, Selenide, and Phosphide Catalysts of Fe, Co, and Ni: A Review, *ACS Catal.*, 2016, **6**, 8069–8097.
15 S. Anantharaj and S. Noda, Nickel selenides as pre-catalysts for electrochemical oxygen evolution reaction: A review, *Int. J. Hydrogen Energy*, 2020, **45**, 15763–15784.
16 X. Xia, L. Wang, N. Sui, V. L. Colvin and W. W. Yu, Recent progress in transition metal selenide electrocatalysts for water splitting, *Nanoscale*, 2020, **12**, 12249–12262.
17 Y. Sun, K. Xu, Z. Wei, H. Li, T. Zhang, X. Li, W. Cai, J. Ma, H. J. Fan and Y. Li, Strong Electronic Interaction in Dual-Cation-Incorporated NiSe2 Nanosheets with Lattice Distortion for Highly Efficient Overall Water Splitting, *Adv. Mater.*, 2018, **30**, 1–7.
18 Y. Chen, J. Zhang, P. Guo, H. Liu, Z. Wang, M. Liu, T. Zhang, S. Wang, Y. Zhou, X. Lu and J. Zhang, Coupled Heterostructure of Mo-Fe Selenide Nanosheets Supported on Carbon Paper as an Integrated Electrocatalyst for Efficient Hydrogen Evolution, *ACS Appl. Mater. Interfaces*, 2018, **10**, 27787–27794.
19 J. Yuan, X. Cheng, H. Wang, C. Lei, S. Pardiwala, B. Yang, Z. Li, Q. Zhang, L. Lei, S. Wang and Y. Hou, A Super-aerophobic Bimetallic Selenides Heterostructure for Efficient Industrial-Level Oxygen Evolution at Ultra-High Current Densities, *Nano-Micro Lett.*, 2020, **12**, 1–12.
20 C. Liu, T. Gong, J. Zhang, X. Zheng, J. Mao, H. Liu, Y. Li and Q. Hao, Engineering Ni_2P-$NiSe_2$ heterostructure interface for highly efficient alkaline hydrogen evolution, *Appl. Catal., B*, 2020, **262**, 1–8.
21 D. Chen, Z. Xu, W. Chen, G. Chen, J. Huang, J. Huang, C. Song, C. Li and K. (Ken) Ostrikov, Just add water to split water: ultrahigh-performance bifunctional electrocatalysts fabricated using eco-friendly heterointerfacing of NiCo diselenides, *J. Mater. Chem. A*, 2020, **8**, 12035–12044.
22 B. Wang, C. Tang, H. F. Wang, X. Chen, R. Cao and Q. Zhang, A Nanosized CoNi Hydroxide@Hydroxysulfide Core–Shell Heterostructure for Enhanced Oxygen Evolution, *Adv. Mater.*, 2019, **31**, 1–7.
23 Y. Li, W. Wang, B. Huang, Z. Mao, R. Wang, B. He, Y. Gong and H. Wang, Abundant heterointerfaces in MOF-derived hollow CoS_2–MoS_2 nanosheet array electrocatalysts for overall water splitting, *J. Energy Chem.*, 2021, **57**, 99–108.
24 C. Zhang, Y. Xue, L. Hui, Y. Fang, Y. Liu and Y. Li, Graphdiyne@$NiO_x(OH)_y$ heterostructure for efficient overall water splitting, *Mater. Chem. Front.*, 2021, **5**, 5305–5311.
25 K. Xiao, L. Zhou, M. Shao and M. Wei, Fabrication of (Ni,Co)0.85Se nanosheet arrays derived from layered double hydroxides toward largely enhanced overall water splitting, *J. Mater. Chem. A*, 2018, **6**, 7585–7591.
26 X. Zhang, Y. Ding, G. Wu and X. Du, $CoSe_2$@$NiSe_2$ nanoarray as better and efficient electrocatalyst for overall water splitting, *Int. J. Hydrogen Energy*, 2020, **45**, 30611–30621.
27 Y. Li, S. Guo, T. Jin, Y. Wang, F. Cheng and L. Jiao, Promoted synergy in core-branch CoP@NiFe–OH nanohybrids for efficient electrochemical-/photovoltage-driven overall water splitting, *Nano Energy*, 2019, **63**, 103821.
28 H. Wang, Q. Fang, W. Gu, D. Du, Y. Lin and C. Zhu, Noble Metal Aerogels, *ACS Appl. Mater. Interfaces*, 2020, **12**, 52234–52250.
29 O. Lori, N. Zion, H. C. Honig and L. Elbaz, 3D metal carbide aerogel network as a stable catalyst for the hydrogen evolution reaction, *ACS Catal.*, 2021, **11**, 13707–13713.
30 Z. Lin, S. Liu, Y. Liu, Z. Liu, S. Zhang, X. Zhang, Y. Tian and Z. Tang, Rational design of Ru aerogel and RuCo aerogels with abundant oxygen vacancies for hydrogen evolution reaction, oxygen evolution reaction, and overall water splitting, *J. Power Sources*, 2021, **514**, 230600.
31 B. Zhang, F. Yang, X. Liu, N. Wu, S. Che and Y. Li, Phosphorus doped nickel-molybdenum aerogel for efficient overall water splitting, *Appl. Catal., B*, 2021, **298**, 120494.
32 L. Liu, L. X. Chen, A. J. Wang, J. Yuan, L. Shen and J. J. Feng, Hydrogen bubbles template-directed synthesis of self-supported AuPt nanowire networks for improved ethanol oxidation and oxygen reduction reactions, *Int. J. Hydrogen Energy*, 2016, **41**, 8871–8880.
33 A. A. Dubale, Y. Zheng, H. Wang, R. Hübner, Y. Li, J. Yang, J. Zhang, N. K. Sethi, L. He, Z. Zheng and W. Liu, High-Performance Bismuth-Doped Nickel Aerogel Electrocatalyst for the Methanol Oxidation Reaction, *Angew. Chem., Int. Ed.*, 2020, **59**, 13891–13899.
34 B. Cai and A. Eychmüller, Promoting Electrocatalysis upon Aerogels, *Adv. Mater.*, 2019, **31**, 1–16.
35 K. Deng, T. Ren, Y. Xu, S. Liu, Z. Dai, Z. Wang, X. Li, L. Wang and H. Wang, Transition metal M (M = Co, Ni, and Fe) and boron co-modulation in Rh-based aerogels for highly efficient

and pH-universal hydrogen evolution electrocatalysis, *J. Mater. Chem. A*, 2020, **8**, 5595–5600.

36 F. Chen, F. Yang, H. Liu, S. Che, G. Zhang, C. Xu and Y. Li, One-pot preparation of surface vulcanization Co-Fe bimetallic aerogel for efficient sulfadiazine degradation, *Chem. Eng. J.*, 2022, **430**, 132904.

37 B. Jansi Rani, G. Ravi, R. Yuvakkumar, B. Saravanakumar, M. Thambidurai, C. Dang and D. Velauthapillai, $CoNiSe_2$-Nanostructures for Clean Energy Production, *ACS Omega*, 2020, **5**, 14702–14710.

38 C. Liu, T. Gong, J. Zhang, X. Zheng, J. Mao, H. Liu, Y. Li and Q. Hao, Engineering Ni2P-NiSe2 heterostructure interface for highly efficient alkaline hydrogen evolution, *Appl. Catal., B*, 2020, **262**, 1–8.

39 A. Badruzzaman, A. Yuda, A. Ashok and A. Kumar, Recent advances in cobalt based heterogeneous catalysts for oxygen evolution reaction, *Inorg. Chim. Acta*, 2020, **511**, 119854.

40 V. D. Nithya, Recent advances in $CoSe_2$ electrocatalysts for hydrogen evolution reaction, *Int. J. Hydrogen Energy*, 2021, **46**, 36080–36102.

41 Y. Yang, W. Zhang, Y. Xiao, Z. Shi, X. Cao and Y. Tang, CoNiSe 2 heteronanorods decorated with layered-double-hydroxides for efficient hydrogen evolution, *Appl. Catal., B*, 2019, **242**, 132–139.

42 X. Yun, T. Lu, R. Zhou, Z. Lu, J. Li and Y. Zhu, Heterostructured NiSe 2/CoSe 2 hollow microspheres as battery-type cathode for hybrid supercapacitors: Electrochemical kinetics and energy storage mechanism, *Chem. Eng. J.*, 2021, **426**, 131328.

43 L. Wei, J. Luo, L. Jiang, L. Qiu, J. Zhang, D. Zhang, P. Xu and D. Yuan, CoSe 2 nanoparticles grown on carbon nanofibers derived from bacterial cellulose as an efficient electrocatalyst for hydrogen evolution reaction, *Int. J. Hydrogen Energy*, 2018, **43**, 20704–20711.

44 V. H. Hoa, D. T. Tran, D. C. Nguyen, D. H. Kim, N. H. Kim and J. H. Lee, Molybdenum and Phosphorous Dual Doping in Cobalt Monolayer Interfacial Assembled Cobalt Nanowires for Efficient Overall Water Splitting, *Adv. Funct. Mater.*, 2020, **30**, 1–12.

45 H. Dau, C. Limberg, T. Reier, M. Risch and S. Roggan, The Mechanism of Water Oxidation: From Electrolysis via Homogeneous to Biological Catalysis, *ChemCatChem*, 2010, **2**, 724–761.

46 I. C. Man, H. Y. Su, F. Calle-Vallejo, H. A. Hansen, J. I. Martínez, N. G. Inoglu, J. Kitchin, T. F. Jaramillo, J. K. Nørskov and J. Rossmeisl, Universality in Oxygen Evolution Electrocatalysis on Oxide Surfaces, *ChemCatChem*, 2011, **3**, 1159–1165.